Realization of Mott-insulating electrides in dimorphic Yb_{5}Sb_{3}

Yangfan Lu, Junjie Wang, Jiang Li, Jiazhen Wu, Shu Kanno, Tomofumi Tada, and Hideo Hosono

Phys. Rev. B **98**, 125128 — Published 14 September 2018

DOI: 10.1103/PhysRevB.98.125128

Realization of Mott Insulating Electrides in Dimorphic Yb_5Sb_3

Yangfan Lu[1†], Junjie Wang[1,2†,#], Jiang Li[1], Jiazhen Wu[1], Shu Kanno[1], Tomofumi Tada[1‡], and Hideo Hosono[1]*

[1]Materials Research Center for Element Strategy, Tokyo Institute of Technology, 4259 Nagatsuta, Midori-ku, Yokohama 226-8503, Japan

[2]International Center for Materials Discovery, School of Materials Science and Engineering, Northwestern Polytechnical University, Xi'an, Shaanxi 710072, People's Republic of China

[†]These authors contributed equally

Corresponding authors

[#]wang.junjie0810@gmail.com

[‡]tada.t.ae@m.titech.ac.jp

*hosono@msl.titech.ac.jp

Abstract

Electrides are exotic compounds that confine anionic electrons in periodically distributed sub-nanometer sized spaces. Such trapped electrons are free from onsite electron-nuclear interaction and exhibit unconventional properties. Here, we report that α- and β-Yb_5Sb_3 are inorganic electrides exhibiting Mott insulating features. Anionic electrons are stabilized in the quasi-one and -zero dimensional spaces, and give rise to the corresponding electride bands near their Fermi levels. Despite the partially occupied electronic picture, both of these systems exhibit semiconducting conductivity and Currie-type magnetism with S = 1/2 moments, demonstrating electron localization. These findings show that anionic electrons can serve as magnetic centers, and inorganic electrides have the potential to act as strongly correlated materials even without the presence of localized atomic orbitals.

Introduction

As is observed in a wide range of insulators, an electron can be trapped at a random anionic vacancy to form an F-center with a spherical wave function [1,2]. Electrons isolated in such ionic cavities are loosely bound to the cationic lattice, giving rise to defect states [2]. The idea of stoichiometric F-centers was extended by Dye et al. to organic salts, which led to the studies of the materials known as electrides [3-7]. Electrides confine a much higher anionic electron density than F-centers, arising extra energy bands near their Fermi levels [7]. These discoveries demonstrated that anionic electrons can be stabilized in bulk materials, and opened the electronic pictures, in which periodically distributed vacancies can be electronically active. However, organic electrides can only be stabilized under low temperatures and an inert gas atmosphere, hindering the further investigation of their properties and application studies [8].

In 2003, Matsuishi et al. synthesized an inorganic electride, $(Ca_{24}Al_{28}O_{64})^{4+}(4e^-)$ (C12A7:e^-), with improved chemical and thermal stability [9]. The crystallographic cage structure of C12A7:e^- can accommodate up to 2×10^{21} cm^{-3} anionic electrons, leading to the realization of a quasi-zero dimensional electride. A further modifying the topology of the trapping space has led to the synthesis of various layered systems, such as Ca_2N, *Ae*AlSi (*Ae* = Ca, Sr, Ba) and Y_2C, showing two-dimensional (2D) electron gas, superconductivity and anionic electron induced magnetism [10-12]. The presence of high anionic electron density distinguishes electrides from the other inorganic materials and provides a promising arena for the emergence of exotic phenomena. In particular, the spin-polarization of Y_2C has drawn considerable attention since anionic electrons serve as magnetic center and significantly affected its properties [13]. Therefore, the further exploration of low-dimensional electrides is significantly important for finding electronic phases with stronger electron correlation, and showing that inorganic electrides can be a unique playground for strongly correlated systems.

Here, we report that α- and β-Yb_5Sb_3 are Mott insulating electrides. While the synthesis of α- and β-Yb_5Sb_3 was reported previously, the detailed physical properties have not been investigated, yet [14,15]. These two compounds contain interstitial sites surrounded by Yb_6 octahedra and Yb_4 tetrahedra, and confine anionic electrons in the quasi-one and -zero dimensional spaces. It is plausible due to the low dimensionality and the half-filled nature, anionic electrons are strongly localized, resulting in semiconducting conductivity and Curie-type magnetism with $S = 1/2$ magnetic moments. Since the contribution of Yb to the Fermi level is smaller than anionic electrons, the dimorphic Yb_5Sb_3 can be categorized as Mott insulating electrides. These discoveries show that electron correlation between anionic electrons play important role in low dimensional electrides, and offer a valuable example of how the periodic cavities can be electronically and magnetically important even without nuclei.

Methods

Polycrystalline α-Yb_5Sb_3 samples were synthesized using conventional solid state reactions as mentioned by Leon-Escamilla et al [14,15]. Elemental powders of Yb and Sb were mixed with the molar ratio of Yb : Sb = 5.4 : 3 and sealed into a stainless tube (SUS316) with Ar gas. The tubes were sintered under Ar flow at 1150 ^{o}C for 2 hours and slowly cooled to 650 ^{o}C for 80 hours. The α-Yb_5Sb_3 samples used for electrical transport measurements were prepared by pelletizing obtained powder with the hydrostatic pressure of 200 MPa without additional heat treatment. Polycrystalline β-Yb_5Sb_3 was obtained by sintering pelletized α-Yb_5Sb_3 powder in stainless tubes at 800 ^{o}C for 40 hours. Polycrystalline β-$Yb_5Sb_3F_x$ was also synthesized using conventional solid state reactions. Elemental powders of Yb, YbF_3 and Sb were mixed with the molar ratio of Yb : Sb : F = 5.4 : 3 : 1 and sealed into a stainless tube (SUS316) with Ar gas. The tubes were sintered under Ar flow at 1150 ^{o}C for 2 hours and slowly cooled to 650 ^{o}C for 80 hours. The obtained powder was pelletized and annealed at 800 ^{o}C for 40 hours. Silica tube is not suitable for each step since Yb reacts with SiO_2, resulting in substantial production of

cubic Yb_4Sb_3. The obtained α-Yb_5Sb_3, β-Yb_5Sb_3 and β-$Yb_5Sb_3F_x$ are colored black and stable in air at least during the measurements, and characterized using Powder X-ray diffraction (XRD). The hydrogen content of sintered Yb_5Sb_3 was measured using temperature programmed H_2 desorption (H_2-TPD). The transport and magnetic properties were measured using commercial PPMS and SVSM (Quantum Design).

Density functional theory (DFT) calculations were performed using the generalized gradient approximation with the Perdew-Burke-Ernzerhof (PBE) functional and the projector augmented plane wave (PAW) method, as implemented in Vienna ab initio simulation package (VASP 5.4.1) [16,17]. The plane wave cut-off was set to 600 eV for each model. Monkhorst-Pack *k*-point grid for the first Brillouin zone sampling was $6 \times 6 \times 8$ for α-Yb_5Sb_3 and $6 \times 5 \times 4$ for β-Yb_5Sb_3. The core electrons were handled in the PAW method, and Valence electrons ($6s^2$ and $5p^6$ electrons of Yb and $5s^2$ and $5p^3$ electrons of Sb) were represented with wave functions based on plane waves, whereas the 4*f* of Yb was represented as core electrons. The convergence criteria of total energy and force were respectively 1.0×10^{-6} eV and 1.0×10^{-3} eV/Å for all models. The atomic positions and lattice parameters of Yb_5Sb_3 compounds were fully optimized, and the validity of the computational conditions was confirmed in the comparison with experimental values. The electronic structure analyses (i.e., band structures, projected density of states, and real space electron density analysis) were performed using the optimized structures.

DFT + *U* approach was employed to the lattice relaxations and electronic structure calculations for α- and β-Yb_5Sb_3 to describe its band gap by applying on-site Coulomb repulsions (Hubbard *U*) of 1, 3 and 5 eV (α-phase) and 5 eV (β-phase) to Yb *d* state. The other settings of DFT + *U* approach are the same with those used in DFT calculations. To get better estimation of band gaps, the screened Hybrid Functional of Heyd, Scuseria and Ernzerhof (HSE) was used to relax the lattices and calculate the electronic structures for both α- and β-Yb_5Sb_3 [18,19]. The

Hartree–Fock mixing parameter and the screening parameter μ were set to 25 % and 0.2 $Å^{-1}$ (HSE06), respectively. A cutoff of 600 eV and *k*-point mesh of $2\pi \times 0.04$ $Å^{-1}$ were used for the relaxations and electronic structure calculations. The obtained lattice constants are $a = b = 8.990$ Å and $c = 6.856$ Å for α-phase and $a = 12.423$ Å, $b = 9.507$ Å and $c = 8.213$ Å for β-phase, respectively, which are in excellent agreement with the experimental values.

Results and discussion

Figures 1 (a) and (b) show the crystal structures of α- and β-Yb_5Sb_3. α-Yb_5Sb_3 crystallizes in the hexagonal Mn_5Si_3-type structure ($P6_3/mcm$). Two Yb sites can be defined in the lattice, and one of the Yb sites comprises Yb_6 octahedral chains along the *c*-axis, forming a large interstitial space (denoted as X in Figure 1). In contrast, the β-Yb_5Sb_3 crystallizes in an orthorhombic structure (Pnma), and Yb atoms constitute Yb_4 tetrahedral cages. This structure also contains an interstitial space X in the tetragonal cage center. It is noteworthy that H^- ions can be stabilized in the site X without accompanying a large modification of their crystal structures [14,15]. The reduced lattice strain due to insertion/extraction of anionic ions is one of the characteristics of electrides. Therefore, the sites X can be regarded as crystallographic sites that may give rise to electride bands as discussed for other electrides [9-13].

In addition to the existence of large interstitial spaces surrounded by the cations, the presence of excess electrons should be highlighted in Yb_5Sb_3 compounds, as can be shown from analysis of their volume in terms of the ionic radii of the constituent Yb and Sb atoms. Figures 1 (c) and (d) show the cube root of volumes ($(V_{cell})^{1/3}$) of Ln_5Sb_3 compounds as a function of ionic radius of *Ln* atoms, where V_{cell} is the unit cell volume and *Ln* represents rare-earth elements. According the previously reported lattice parameters, the $(V_{cell})^{1/3}$ values of the Ln_5Sb_3 linearly decrease with increasing atomic number of *Ln* due to lanthanide contraction, and fall into a universal line by assuming the trivalent states of *Ln* ions [20-29]. The trivalent states of the *Ln* ions were also

confirmed by magnetization measurements [28]. In contrast, the data for the α- and β-Yb_5Sb_3 show a distinct deviation from the fitted line obtained using the ionic radius of trivalent Yb but agree well with the fitting by assuming that the Yb occurs as divalent state. It is not surprising that divalent state is stabilized in Yb since Yb^{2+} satisfies the situation of fully occupied 4*f* orbitals, and Yb^{2+} states can be universally stabilized in oxides and halides [30,31]. The presence of one excess electron per formula unit (f.u.) is therefore expected in Yb_5Sb_3 with a formal valence state of $(Yb_5Sb_3)^+(e^-)$.

The co-existence of interstitial sites and excess electron picture are reminiscent of previously reported electrides, and motivated us to investigate the dimorphic Yb_5Sb_3 as electride candidates. To examine the origin of excess electrons in the electronic structure, we first conducted DFT calculations on the hypothetic α- and β-Yb_5Sb_3H as the parent compounds. As depicted in Figures 2 (a) and (b), α- and β-Yb_5Sb_3H are predicted to be semi-metallic and semiconducting, respectively. In both materials, the lowest conduction band dominantly originates from the Yb 5*d* orbitals, whereas the valence bands include significant contribution from Sb 5*p* orbitals together with the H 1*s* states located at 3.0 ~ 5.0 eV and at 4.0 ~ 4.5 eV below the Fermi level in α- and β-Yb_5Sb_3H, respectively [Figure 2 (a), (b) and Figure 12 in the Appendix B]. These results roughly yield a formal valence state configuration of $(Yb_5Sb_3)^+(H^-)$, and are consistent with unit cell volume dependence of the *Ln* site cations, supporting that Yb^{2+} and Sb^{3-} are stabilized.

The calculated band structures of Yb_5Sb_3, by contrast, are metallic [Figures 2 (c) and (d)]. Since the extraction of H^- as H^0 species serve as electron doping ($H^- \rightarrow 1/2\ H_2 + e^-$), the doped electrons would be transferred into the conduction band. In contrast to the rigid band concept, DFT calculations revealed that extra energy bands (two in α- and four in β-phase) appear at the Fermi level after H^- extraction, whereas the conduction and valence bands remain largely

unchanged. The emergence of the extra bands (electride bands) suggests that the doped electrons are not transferred into the conduction band but rather are retained at the sites originally occupied by the H^- ions (Figure 13 in the Appendix B). The charge densities of these confined electrons are nodeless, and the number of electride bands is equal to that of the X sites. Furthermore, band dispersion of the electride bands is roughly the same as that of the H 1*s* bands of Yb_5Sb_3H (Figure 2), suggesting that the orbital symmetry is largely unchanged between them. The electron density of each void is equally distributed (Figure 13 in the Appendix B), indicating that the half-filled situation is realized. These results agree well with the electride picture in which one interstitial site gives rise to one electride band, whereas other atomic orbitals play smaller contributions.

Interestingly, the band structures of α- and β-Yb_5Sb_3 can be affected by spin-polarization. Total energies of α- and β-Yb_5Sb_3 were stabilized in the anti-ferromagnetic (AFM) configuration (Figure 3), and their electride bands were found to split (Figure 14 and 15 in the Appendix B). For the α-phase, the gap formation could be further promoted by applying Hubbard *U*. With applying Hubbard *U* on the Yb *d* orbitals, the band overlap at the Fermi level of α-Yb_5Sb_3 becomes smaller for U = 1 and 3 eV, and a 0.02 eV gap opens with a *U* value of 5 eV [Figure 4 (a), (c) and Figure 14]. The Hubbard *U* value was consistent with that used in a previous study for $Yb_2Ti_2O_7$ [32]. The similar electronic structure, including gap opening, is also confirmed in β-Yb_5Sb_3 by introducing spin-polarization. For the β-Yb_5Sb_3, a band gap (E_g) of 0.07 eV appears by only using anti-ferromagnetic configuration [Figure 4 (b), (d)], very similar to a typical Mott insulator, e.g. NiO [33]. The larger band gap realized in β-Yb_5Sb_3 is likely due to longer separation of anionic electrons (3.5 Å for α-phase and 6.3 Å for β-phase), which results in lower dimensional nature and thus stronger electron localization.

Different from α-phase, we found that the band gap was not enhanced in β-Yb_5Sb_3 despite Coulomb U was applied (Figure 15). This indicates that while DFT (+ U) calculations are useful to unveil the feature of electron localization, these are not so suitable to interpret the properties of electrides since on-site Coulomb U cannot be introduced to interstitial sites directly. Therefore, to confirm the formation and calculate E_g of α- and β-Yb_5Sb_3 more precisely, we adopted the screened hybrid functionals (HSE06) in the band structure calculations [18,19]. The E_g of α- and β-Yb_5Sb_3 were respectively estimated as 0.04 and 0.37 eV within HSE functionals (Figure 5), showing a consistent trend with DFT + U calculations. The calculated DOS are similar between DFT + U and HSE06 (Figure 4 and 5), and revealed that the contributions from the interstitial electrons are dominant for the electride bands. Indeed, the real space electron density analysis showed that localized electrons exist at the interstitial sites [Figures 4 (e) and (f)]. More importantly, magnetic moments of α- and β-Yb_5Sb_3 are mainly located at interstitial sites, i.e. ~97 % for α- and ~63 % for β-Yb_5Sb_3 (Figure 6). The magnetic moments are smaller at Yb sites (e.g. Yb1 and Yb2) in α-phase, whereas the Yb sites (e.g. Yb1, Yb2, Yb3 and Yb4) in the β-phase show larger polarization plausibly due to the smaller cage volume of Yb_4 tetrahedra, which induce orbital hybridization between anionic electrons and Yb 5*d* orbitals. Given the fact that anionic electrons play major contribution to magnetic moments, α- and β-Yb_5Sb_3 compounds can be regarded as Mott insulating electrides, in which anionic electrons serve as localized magnetic center.

The insulating natures of α- and β-Yb_5Sb_3 were experimentally confirmed from electronic transport and magnetic properties measurements. Figure 7 illustrates the temperature dependence of electrical resistivity data of the α- and β-Yb_5Sb_3. The resistivity value of α-Yb_5Sb_3 is as large as ~10^1 Ωcm at 300 K and monotonically increases with lowering temperature, reaching ~10^4 Ωcm at 2 K, yielding transport activation energy (E_a) of 0.07 eV. β-

Yb_5Sb_3 exhibits a larger resistivity than that of the α-phase, and its E_a was estimated to be 0.10 eV. These measured E_a indicates the energy difference between the bottom of conduction band and Fermi level. Thus, the E_g of α- and β-Yb_5Sb_3 can be respectively estimated as $E_g \sim 0.14$ and $E_g \sim 0.20$ eV. These values and tendencies are consistent with the results calculated within HSE06 functionals (0.04 and 0.37 eV for α- and β-Yb_5Sb_3). No phase transitions can be identified in both compounds at least within the measurement temperature range.

Magnetization measurements provided a further confirmation of the presence of localized anionic electrons. As shown in Figure 8, both α- and β-Yb_5Sb_3 exhibit Curie-type magnetism. To subtract the contribution of ferromagnetic impurities, we defined χ as $\chi = [M(3T) - M(1T)] / B(2T)$. The χ^{-1} can be well fitted using a Curie–Weiss plot, and their effective magnetic moments (μ_{eff}) and Weiss temperatures (θ_W) were estimated to be $\mu_{eff} = 1.7\ \mu_B$ per f.u. and $\theta_W = -17.6$ K for the α-phase and $\mu_{eff} = 2.1\ \mu_B$ per f.u. and $\theta_W = -10.7$ K for the β-phase. Both of the obtained μ_{eff} are far smaller than the magnetic moments of Yb^{3+} ions (~10 μ_B per f.u.) but are rather consistent with $S = 1/2$ moments confined in the periodically distributed voids, demonstrating the absence of 4*f* electrons. The negative θ_W values imply the presence of an anti-ferromagnetic interaction between the anionic electrons, consistent with computational prediction (Figure 3). The calculated μ_{eff} are qualitatively consistent with experimentally obtained values, but 45 % (α-phase) and 20 % (β-phase) smaller than experimentally obtained values (Figure 6). The calculated μ_{eff} may be underestimated since hybrid functional method used in present study is still not perfect to describe the strong correlation effect between anionic electrons, which is more significant in α-phase due to the shorter separation between interstitial sites X [Figure 1 (a) and (b)].

The physical properties of Yb_5Sb_3 are sensitive to the X-site occupancy (Figure 9). In this experiment we inserted F atoms to interstitial sites instead of H since controlling of H content was difficult. The transport activation energy was estimated to be $E_a \sim 0.25$ eV and roughly gives the band gap to be $E_g \sim 0.50$ eV by F insertion, while the μ_{eff} was suppressed to $\mu_{eff} \sim 1\ \mu_B$. The μ_{eff} is reduced since anionic electrons form spin-singlet state via F insertion as expressed by $(Yb_5Sb_3)^+(e^-) + 1/2\ F_2 \rightarrow (Yb_5Sb_3)^+(F^-)$. This will result in a transformation from a Mott to a conventional band insulator. The experimentally estimated E_g is smaller than that of DFT calculations ($E_g \sim 0.8$ eV) in β-Yb_5Sb_3F (Figure 16 and 17 in the Appendix B), suggesting the presence of partially survived anionic electrons associated with the presence of F vacancies. Indeed, the hybrid functional calculations of β-$Yb_5Sb_3F_{0.75}$, β-$Yb_5Sb_3F_{0.5}$, β-$Yb_5Sb_3F_{0.25}$, showed that F deficiencies of β-$Yb_5Sb_3F_x$ resulted in smaller band gaps and presence of residual magnetic moments (Figure 16 and 17 in the Appendix B). By comparing the variations of measured E_g and μ_{eff} with those calculated results, we can suggest the obtained sample is close to β-$Yb_5Sb_3F_{0.5}$. The calculated spin density of β-$Yb_5Sb_3F_{0.5}$ shows that its magnetic moment still originates from the strong localized anionic electrons (Figure 17 in the Appendix B).

Both experimentally and computationally obtained results showed that electron correlation between anionic electrons plays important role in α- and β-Yb_5Sb_3. Two factors can maximize electron correlation between anionic electrons. First, the half-filled states are considered to be a key for the realization of a Mott insulating state. As discussed in the phase diagram, the half-filled states are favored to realize Mott insulates, whereas the systems become more metallic as band filling departs from half-filled situation [34]. The well-studied C12A7:e^- electride exhibits metallic conductivity because it only confines 1/3 electrons per vacant site and can be interpreted as a heavily hole-doped system starting from the half-filled state [9]. Second, the low dimensionality should play another key role to further enhance electron correlation effect.

The α- and β-Yb_5Sb_3 can be categorized as quasi-one and -zero dimensional electrides, and it is known that lower dimensionality enhances electron correlation due to reduced band width [35,36]. The layered electrides, such as Ca_2N and Y_2C, are therefore considered to exhibit metallic conductivity despite the half-filled picture and similar X–X distances with α-Yb_5Sb_3 [10,11]. It is noted that the electronic structures of Yb_5Sb_3 are similar to the previously studied anti-ferromagnetic, $(A)_8(AlSiO_4)_6$ (A = alkali metals), in which F-center electrons are periodically confined in the $(Na/K)_4$ tetrahedral cages [37,38]. It was considered that interstitial electron bands of $(A)_8(AlSiO_4)_6$ are half-filled and show small dispersion plausibly due to quasi-zero dimensional nature, and as a consequence, $(A)_8(AlSiO_4)_6$ were considered to realize Mott insulating state. The co-existence of half-filled and low-dimensional natures also present in dimorphic Yb_5Sb_3 and thus strong electron localization can be realized.

Spin-density-wave (SDW), associated with the low-dimensional electronic feature, is unlikely to interpret the insulating nature in Yb_5Sb_3 compounds. Below T_c, a SDW transition develops anti-ferromagnetic ordering together with a formation of band gaps from where nesting vector exists [39]. In the high temperature phase of SDW, the system is a paramagnetic metal and would transform to a magnetic insulator with the decrease of temperature. In α- and β-Yb_5Sb_3, by contrast, the systems are insulating even in the paramagnetic states (Figure 7 and 8), showing the absence of Fermi surface and nesting vector. Therefore, SDW transitions cannot explain the insulating natures of Yb_5Sb_3, but electron correlation.

Finally, we turn to the possibility of extending of Mott insulating electrides concept to a wider range of compounds. It is noted that other families of compounds, such as Ba_5Sb_3 and Sr_5P_3, were also reported to manifest insulating states [40-42]. Both of them host $Ba(Sr)_6$ octahedral cages that constitute interstitial sites. The band gaps were reported to be 0.3 and 0.1 eV for Ba_5Sb_3 and Sr_5P_3, respectively. Furthermore, 1.6 μ_B of magnetic moment was reported for

Ba_5Sb_3, comparable to those of α-Yb_5Sb_3 [40,42]. While Zintl concept was considered to explain the unconventional transport properties, the relatively long polymeric anion distance (Sb–Sb: ~4.5 Å) leaves open the question on the real electronic origin for its semiconducting nature. Moreover, the presence of magnetic moments is in contrast to the Zintl concept, in which the valence electrons form a spin-singlet state through chemical bondings. Therefore Ba_5Sb_3 and Sr_5P_3 are considered to have similar electronic structures to Yb_5Sb_3, and strongly localized anionic electrons may be universally observed in low dimensional electrides.

Conclusions

In summary, a combined approach of computational calculations, transport and magnetic measurements revealed the electronic origin of the insulating state of α- and β-Yb_5Sb_3 and interpreted the results in terms of localized anionic electrons. Our work unveiled that Yb_5Sb_3 compounds are air-stable electrides, and they host localized anionic electrons in the Yb_6 octahedra of α-phase and Yb_4 tetrahedra of β-phase that serve as magnetic centers. Their electron correlation is maximized due to the half-filled and low-dimensional nature, leading to the manifestation of Mott insulating electrides. These findings cannot be interpreted within the models, in which the *d* or *f* orbitals play essential roles, and therefore deliver an understanding that applies the anionic electron concept to the strongly correlated materials.

ACKNOWLEDGMENTS

This work was supported by funds from the Accelerated Innovation Research Initiative Turning Top Science and Ideas into High-Impact Values (ACCEL) program of the Japan Science and Technology Agency (JST), and Kakenhi Grant-in-Aid (No.15H04183 & 17H06153) from the Japan Society for the Promotion of Science (JSPS). Y. F. Lu is supported by JSPS research fellowship for young scientist (No. 18J00745).

Y. F. Lu and J. Wang contributed equally to this work.

APPENDIX A: Sample characterization

Powder X-ray diffraction (XRD) patterns were collected on a Bruker D8 Advance diffractometer with Cu Kα radiation at room temperature (Figure 10). The obtained spectra were well refined using the Mn_5Si_3-type ($P6_3/mcm$, #187) and β-Yb_5Sb_3-type (Pnma, #62) structures. The refined lattice parameters were $a = b = 9.029(1)$ Å and $c = 6.900(8)$ Å for α-phase, $a = 12.362(2)$ Å, $b = 9.583(5)$ Å and $c = 8.281(1)$ Å for β-phase, consistent with previously reported values. The lattice parameters of β-$Yb_5Sb_3F_x$ are estimated to be $a = 12.438(0)$ Å, $b = 9.710(3)$ Å and $c = 8.347(4)$ Å. No hydrogen insertions can be confirmed within an H_2-TPD measurement (Figure 11).

APPENDIX B: Computational calculations

Figure 12 illustrates the calculated DOS of α-Yb_5Sb_3H and β-Yb_5Sb_3H with PBE functional, showing that valence bands are composed of Sb 5*p* and H 1*s* orbitals while Yb 5*d* orbitals dominantly contribute to conduction bands. The partial electron densities for α-Yb_5Sb_3 and β-Yb_5Sb_3 are shown in Figure 13. Figure 14 and 15 show the calculated band structure of α- and β-Yb_5Sb_3 with anti-ferromagnetic setting and Hubbard *U*. Figure 16 shows the calculated band structures of β-Yb_5Sb_3F, β-$Yb_5Sb_3F_{0.75}$, β-$Yb_5Sb_3F_{0.50}$ and β-$Yb_5Sb_3F_{0.25}$. Conventional DFT calculation was applied for β-Yb_5Sb_3F, while HSE functionals with anti-ferromagnetic setting were employed for β-$Yb_5Sb_3F_{0.75}$, β-$Yb_5Sb_3F_{0.50}$ and β-$Yb_5Sb_3F_{0.25}$. The calculated band gaps, magnetic moments and spin density distribution of β-$Yb_5Sb_3F_x$ were summarized in Figure 17.

REFERENCES

1. D. L. Dexter, *Phys. Rev.* **83**, 435 (1951).
2. F. Karsai, P. Tiwald, R. Laskowski, F. Tran, D. Koller, S. Gräfe, J. Burgdörfer, L. Wirtz, and P. Blaha, *Phys. Rev. B* **89**, 125429 (2014).
3. J. L. Dye, *Science* **247**, 663 (1990).
4. S. G. Dale, A. Otero-de-la-Roza, and E. R. Johnson, *Phys. Chem. Chem. Phys.* **16**, 14584 (2014).
5. J. L. Dye, *Science* **247**, 663 (1990).
6. Ellaboudy, J. L. Dye, and P. B. Smith, *J. Am. Chem. Soc*. 105, 6490 (1983).
7. S. G. Dale, A. Otero-de-la-Roza, and E. R. Johnson, *Phys. Chem. Chem. Phys.* **16**, 14584 (2014).
8. M. J. Wagner, R. H. Huang, J. L. Eglin, and J. L. Dye, *Nature* **368**, 726 (1994).
9. S. Matsuishi, Y. Toda, M. Miyakawa, K. Hayashi, T. Kamiya, M. Hirano, I. Tanaka, H. Hosono, *Science* **301**, 626 (2003).
10. K. Lee, S. W. Kim, Y. Toda, S. Matsuishi, and H. Hosono, *Nature* **494**, 336 (2013).
11. X. Zhang, Z. Xiao, H. Lei, Y. Toda, S. Matsuishi, T. Kamiya, S. Ueda, and H. Hosono, *Chem. Mater.* **26**, 6638 (2014).
12. Y. F. Lu, T. Tada, Y. Toda, S. Ueda, J. Wu, J. Li, K. Horiba, H. Kumigashira, Y. Zhang, and H. Hosono, *Phys. Rev. B* **95**, 125117 (2017).
13. J. Park, K. Lee, S. Y. Lee, C. N. Nandadasa, S. Kim, K. H. Lee, Y. H. Lee, H. Hosono, S. G. Kim, and S. W. Kim, *J. Am. Chem. Soc*. **139**, 615 (2017).
14. E. A. Leon-Escamilla, and J. D. Corbett, *Chem. Mater*. **18**, 4782 (2006).
15. E. A. Leon-Escamilla, and J. D. Corbett, *J. Alloys Compd*. **265**, 104 (1998).
16. J. P. Perdew, K. Burke, and M. Ernzerhof, *Phys. Rev. Lett.* **77**, 3865 (1996).
17. G. Kresse, G, and J. Furthmu□ller, Phys. Rev. B 54, 11169 (1996).
18. J. Heyd, G. E. Scuseria, and M. Ernzerhof, *J. Chem. Phys.* **118**, 8207 (2003)

19. J. Heyd, G. E. Scuseria, and M. Ernzerhof, *J. Chem. Phys.***124**, 219906 (2006).

20. G. D. Brunton, and H. Steinfink, *Inorg. Chem*. **10**, 2301 (1971).

21. R. E. Bodnar, and H. S. Steinhnk, *Inorg. Chem*. **6**, 327 (1967).

22. W. Rieger, and E. Parthé, *Acta Crystal*. **B24**, 456 (1968).

23. M. N. Abdusaljamova, V. D. Abulchaev, R. Z. Levitin, A. S. Markosijan, V. F. Popov, and R. Yumaguzhin, *J. Less-Common Metals***120**, 281 (1986).

24. M. Zelinska, O. Zhak, S. Oryshchyn, V. Babizhetskyy, J. Y. Pivan, and R. Guerin, *J. Alloys Compd.* 437, 133 (2007).

25. F. A. Schmidt, and O. D. McMasters, *J. Less-Common Metals* 21, 415 (1970).

26. S. Gupta, E. A. León-Escamilla, F. Wang, G. J. Miller, and J. D. Corbett, *Inorg. Chem.* **48**, 4362 (2009).

27. Y. Mozharivskyj, and H. F. Franzen, *J. Alloys Compd*. **319**, 100 (2001).

28. J. K. Yakinthos, and I. P. Semitelou, *J. Mag. Mag. Mater.* **36**, 136 (1983).

29. R. D. Shannon, Acta Cryst. **A32**, 751 (1976).

30. C. A. Voos-Esquivel, and H. A. Eick, *J. Solid State Chem.* **67**, 291 (1987).

31. M. Henke, J. Perßon, and S. Kück, *J. Luminescence* **87–89**, 1049 (2000).

32. N. Deilynazar, E. Khorasani, M. Alaei, and S. J. Hashemifar, *J. Mag. Mag. Mater.* **393**, 127 (2015).

33. C. Rödl, F. Fuchs, J. Furthmüller, and F. Bechstedt, *Phys. Rev. B* **79**, 235114 (2009).

34. M. Imada, A. Fujimori, and Y. Tokura, *Rev. Mod. Phys*. **70**, 1039 (1998).

35. J. Kishine, and K. Yonemitsu, *Int. J. Mod. Phys. B* **16**, 711 (2002).

36. Z. Wang, M. Okude, M. Saito, S. Tsukimoto, A. Ohtomo, M. Tsukada, M. Kawasaki, and Y. Ikuhara, *Nat. Commun*. **1**, 106 (2010).

37. T. Nakano, R. Suehiro, A. Hanazawa, K. Watanabe, I. Watanabe, A. Amato, F. L. Pratt, and Y. Nozue, *J. Phys. Soc. Jpn*. **79**, 073707 (2010).

38. G. K. H. Madsen, B. B. Iversen, P. Blaha, and K. Schwarz, *Phys. Rev. B* **64**, 195102 (2001).

39. G. Grüner, *Rev. Mod. Phys*. **66**, 1 (1994).

40. L. Wolfe, SciTech Connect, available at http://dx.doi.org/10.2172/6824583 (1990).

41. J. Wang, K. Hanzawa, H. Hiramatsu, J. Kim, N. Umezawa, K. Iwanaka, T. Tada, H. Hosono, *J. Am. Chem. Soc.* 139, 15668 (2017).

42. E. A. León-Escamilla, *Iowa State University Digital Repository*, available at http://lib.dr.iastate.edu/rtd/11547/ (1996).

Figure captions

Figure 1. The crystal structures of (a) α-Yb_5Sb_3 and (b) β-Yb_5Sb_3. Yb and Sb atoms are depicted using green and blue spheres, respectively. The $(V_{cell})^{1/3}$ of (c) α-Ln_5Sb_3 and (d) β-Ln_5Sb_3 phases as a function of ionic radius of *Ln* ions. The black dashed line represents line fitting of Ln_5Sb_3 with trivalent *Ln*. The V_{cell} data for α- and β-Ln_5Sb_3 were reported in the Refs. [20-29].

Figure 2. The calculated band structures of (a) α-Yb_5Sb_3H (b) β-Yb_5Sb_3H (c) α-Yb_5Sb_3 and (d) β-Yb_5Sb_3. The components of H 1*s* orbitals in (a) and (b), and anionic electrons in (c) and (d) are represented using red color in the band structure.

Figure 3. The total energy of α-Yb_5Sb_3 and β-Yb_5Sb_3 as a function of each magnetic state. Anti-ferromagnetic configuration is most stable for each system. Red and black circle indicate the data of α-Yb_5Sb_3 and β-Yb_5Sb_3, respectively.

Figure 4. The calculated band structures (a and b), density of states (c and d) and partial charge densities (e and f) of α-Yb_5Sb_3 (a, c and e) and β-Yb_5Sb_3 (b, d and f) using anti-ferromagnetic configuration. The introduced Hubbard *U* was 5 eV for α-Yb_5Sb_3 and 0 eV for β-Yb_5Sb_3. The contributions of electrides states are depicted using solid green (spin-up) and dashed green (spin-down) lines in (c) and (d). The isosurface values of partial charge densities in (e) and (f) are 0.002 and 0.003 e/Bohr^3, respectively. Yb and Sb atoms are depicted using green and blue spheres, respectively.

Figure 5. Calculated band structures and density of states of α-Yb_5Sb_3 (a and c) and β-Yb_5Sb_3 (b and d) using HSE functionals with anti-ferromagnetic setting. Red and Blue dots represent spin-up and spin-down bands.

Figure 6. The spin density distribution of (a) α-Yb_5Sb_3 and (c) β-Yb_5Sb_3 calculated using HSE functionals. The estimated total magnetic moments of each atomic site was summarized in (b) for α-phase and (d) for β-phase, respectively. Yb and Sb atoms are depicted using green and blue spheres, respectively.

Figure 7. Electrical resistivity of (a) α-Yb_5Sb_3 and β-Yb_5Sb_3 and (b) corresponding Arrhenius plots. The transport activation energies (E_a) were respectively estimated to be $E_a \sim 0.07$ eV for α-phase (red) and $E_a \sim 0.10$ eV for β-phase (blue). The black dashed lines represent line fitting.

Figure 8. Magnetic susceptibility of (a) α-Yb_5Sb_3 and β-Yb_5Sb_3. Corresponding χ^{-1} plots are shown in (b). The effective moments (μ_{eff}) were respectively estimated to be $\mu_{eff} \sim 1.7\ \mu_B$ for α-phase (red) and $\mu_{eff} \sim 2.1\ \mu_B$ for β-phase (blue). The black dashed lines represent line fitting.

Figure 9. (a) Electrical resistivity (b) corresponding Arrhenius plots (c) magnetic susceptibility and (d) χ^{-1} plot of β-$Yb_5Sb_3F_x$. The data of β-Yb_5Sb_3 are also shown as blue solid squares for comparisons. The transport activation energy (E_a) and effective moment (μ_{eff}) of β-$Yb_5Sb_3F_x$ were estimated to be $E_a \sim 0.25$ eV and $\mu_{eff} \sim 1\ \mu_B$. Transport data were normalized at 390 K for β-$Yb_5Sb_3F_x$ and 300 K for β-Yb_5Sb_3 in the Arrhenius plots.

Figure 10. Powder XRD diffraction of (a) α-Yb_5Sb_3 (b) β-Yb_5Sb_3 and (c) β-$Yb_5Sb_3F_x$. The reliability parameters are R_{wp} = 9.456 % (S = 1.987) for α-Yb_5Sb_3 and R_{wp} = 9.274 % (S = 1.925) for β-Yb_5Sb_3 and R_{wp} = 11.863 % (S = 2.577) for β-$Yb_5Sb_3F_x$.

Figure 11. H_2-TPD spectrum of sintered Yb_5Sb_3. Clear H_2 desorption could not be confirmed below 800 °C.

Figure 12. Calculated DOS of (a) α-Yb_5Sb_3H and (b) β-Yb_5Sb_3H using PBE functionals. The contribution of Yb, Sb and H orbitals are respectively represented.

Figure 13. Calculated partial electron densities near Fermi levels of (a) α-Yb_5Sb_3 and (b) β-Yb_5Sb_3 using PBE functional. Yb and Sb atoms are depicted using green and blue spheres, respectively. The yellow bubbles represent the electron density in the interstitial sites.

Figure 14. The DFT + U calculations of α-Yb_5Sb_3. (a) Calculated band structures of α-Yb_5Sb_3 with non-spin polarized configuration. Calculated band structures of α-Yb_5Sb_3 with anti-ferromagnetic setting and Hubbard U values of (b) 0 eV (c) 1 eV and (d) 3 eV.

Figure 15. The DFT + U calculations of β-Yb_5Sb_3. Calculated band structures of β-Yb_5Sb_3 with anti-ferromagnetic setting and Hubbard U values of (a) 0 eV (b) 5 eV.

Figure 16. The band calculations on β-$Yb_5Sb_3F_x$. Calculated band structures of β-$Yb_5Sb_3F_x$ with x values of (a) 1.0 (b) 0.75 (c) 0.50 and (d) 0.25. Conventional DFT calculation was conducted for x = 1.0, while HSE functionals were employed for x = 0.75, 0.50 and 0.25.

Figure 17. The band gaps (E_g) and magnetic moments (μ_{eff}) as a function of F content. (a) The summary of E_g and μ_{eff} of β-$Yb_5Sb_3F_x$. The (b) shows the real space spin density distribution of $Yb_5Sb_3F_{0.5}$. Yb, Sb and F atoms are depicted using green, blue and grey spheres, respectively.

Figures

Figure 1

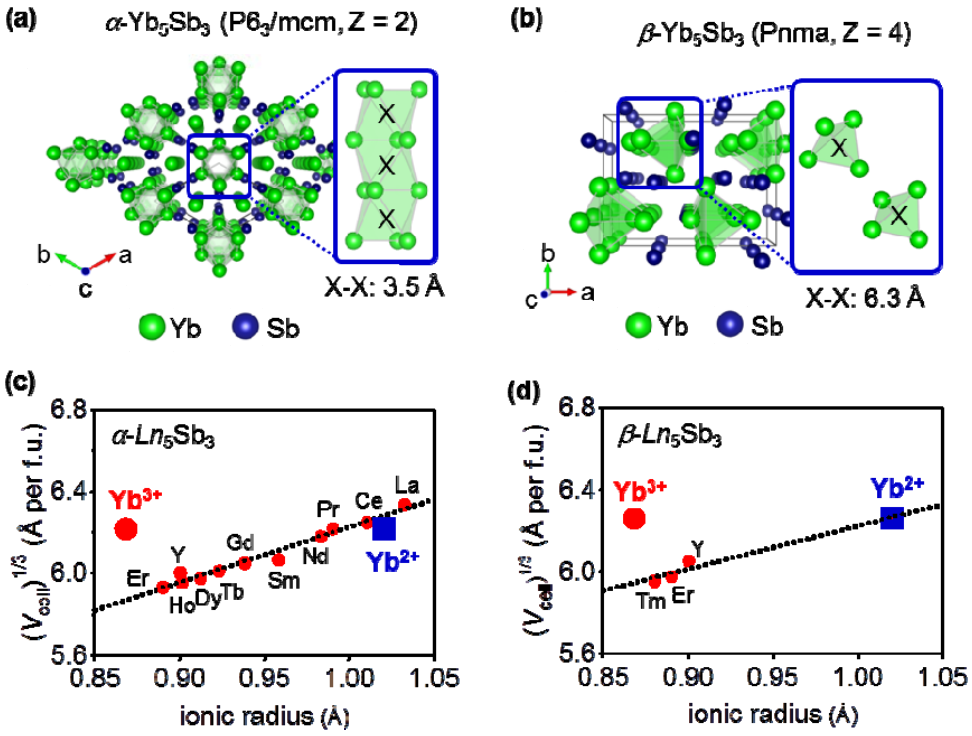

Figure 2

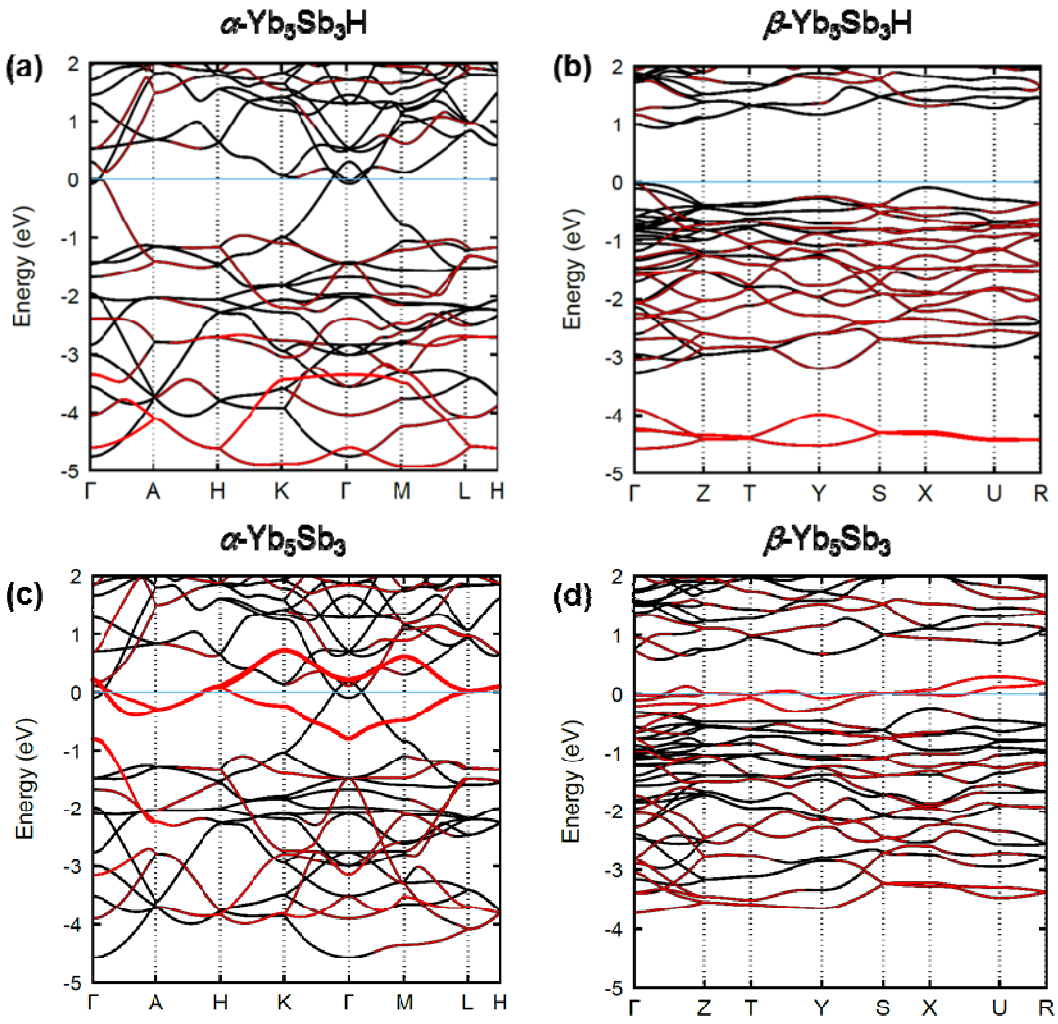
α-Yb5Sb3H
(a)
Energy (eV)
Γ A H K Γ M L H
β-Yb5Sb3H
(b)
Energy (eV)
Γ Z T Y S X U R
α-Yb5Sb3
(c)
Energy (eV)
Γ A H K Γ M L H
β-Yb5Sb3
(d)
Energy (eV)
Γ Z T Y S X U R

Figure 3

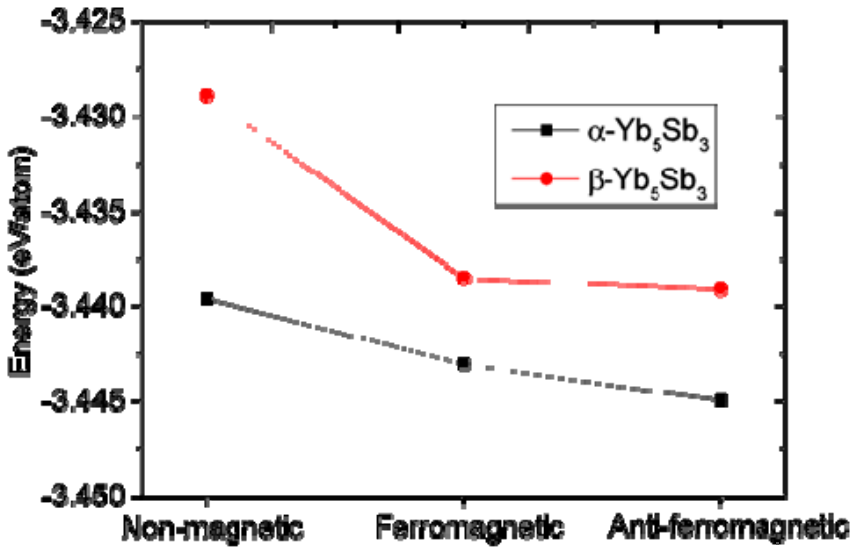
-3.425
-3.430
-3.435
-3.440
-3.445
-3.450
Energy (eV/atom)
α-Yb5Sb3
β-Yb5Sb3
Non-magnetic
Ferromagnetic
Anti-ferromagnetic

Figure 4

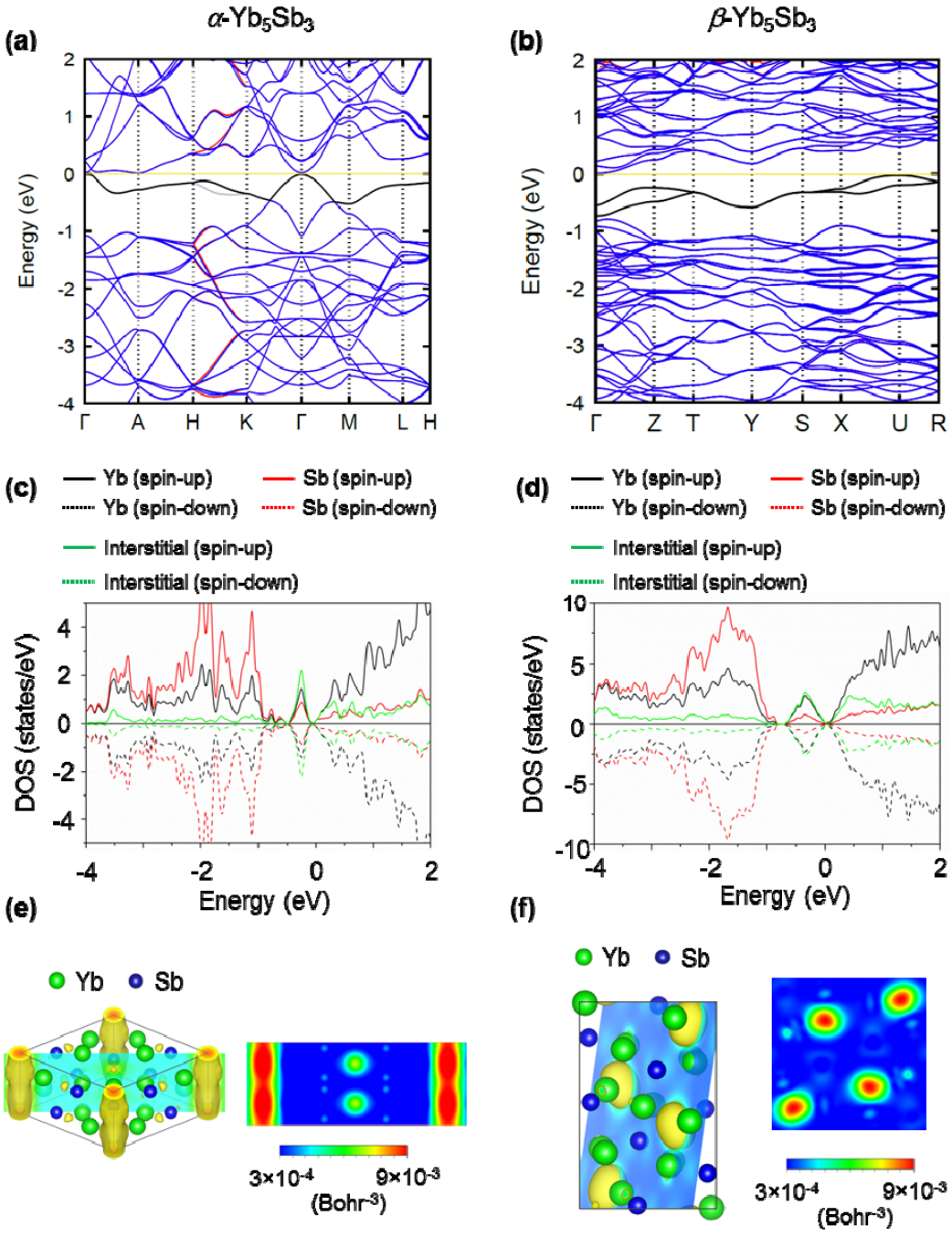
(a)
α-Yb5Sb3
Energy (eV)
Γ A H K Γ M L H
(b)
β-Yb5Sb3
Energy (eV)
Γ Z T Y S X U R
(c)
Yb (spin-up)
Yb (spin-down)
Sb (spin-up)
Sb (spin-down)
Interstitial (spin-up)
Interstitial (spin-down)
DOS (states/eV)
Energy (eV)
(d)
Yb (spin-up)
Yb (spin-down)
Sb (spin-up)
Sb (spin-down)
Interstitial (spin-up)
Interstitial (spin-down)
DOS (states/eV)
Energy (eV)
(e)
Yb
Sb
3×10-4
9×10-3
(Bohr-3)
(f)
Yb
Sb
3×10-4
9×10-3
(Bohr-3)

Figure 5

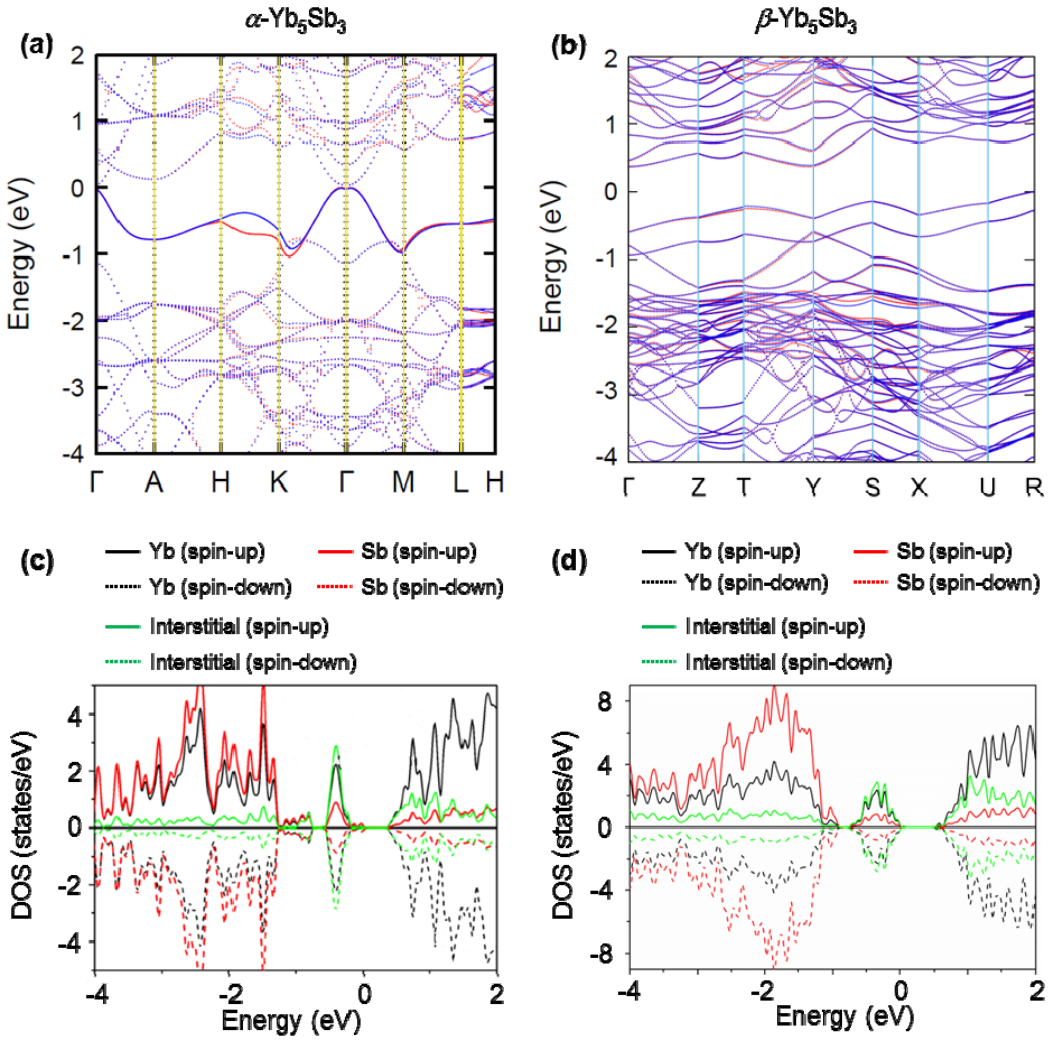
(a)
α-Yb5Sb3
Energy (eV)
Γ A H K Γ M L H
(b)
β-Yb5Sb3
Energy (eV)
Γ Z T Y S X U R
(c)
Yb (spin-up)
Sb (spin-up)
Yb (spin-down)
Sb (spin-down)
Interstitial (spin-up)
Interstitial (spin-down)
DOS (states/eV)
Energy (eV)
(d)
Yb (spin-up)
Sb (spin-up)
Yb (spin-down)
Sb (spin-down)
Interstitial (spin-up)
Interstitial (spin-down)
DOS (states/eV)
Energy (eV)

Figure 6

(a) α-Yb_5Sb_3

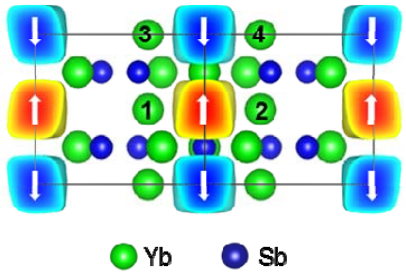

(b)

Atomic site	Total magnetic moments (μ_B)
interstitial X (spin up)	0.919
Yb1	0.012
Yb2	0.012
interstitial X (spin down)	-0.919
Yb3	-0.012
Yb4	-0.012

(c) β-Yb_5Sb_3

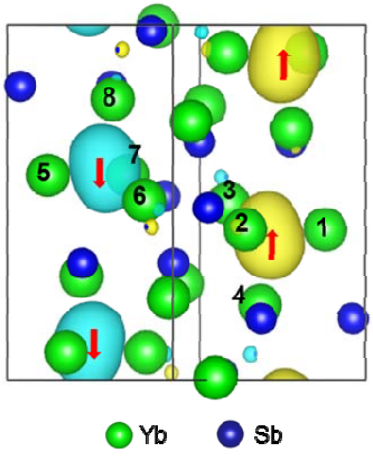

(d)

Atomic site	Total magnetic moments (μ_B)
interstitial X (spin up)	1.060
Yb1	0.168
Yb2	0.168
Yb3	0.168
Yb4	0.121
interstitial X (spin down)	-1.060
Yb5	-0.168
Yb6	-0.168
Yb7	-0.168
Yb8	-0.121

Figure 7

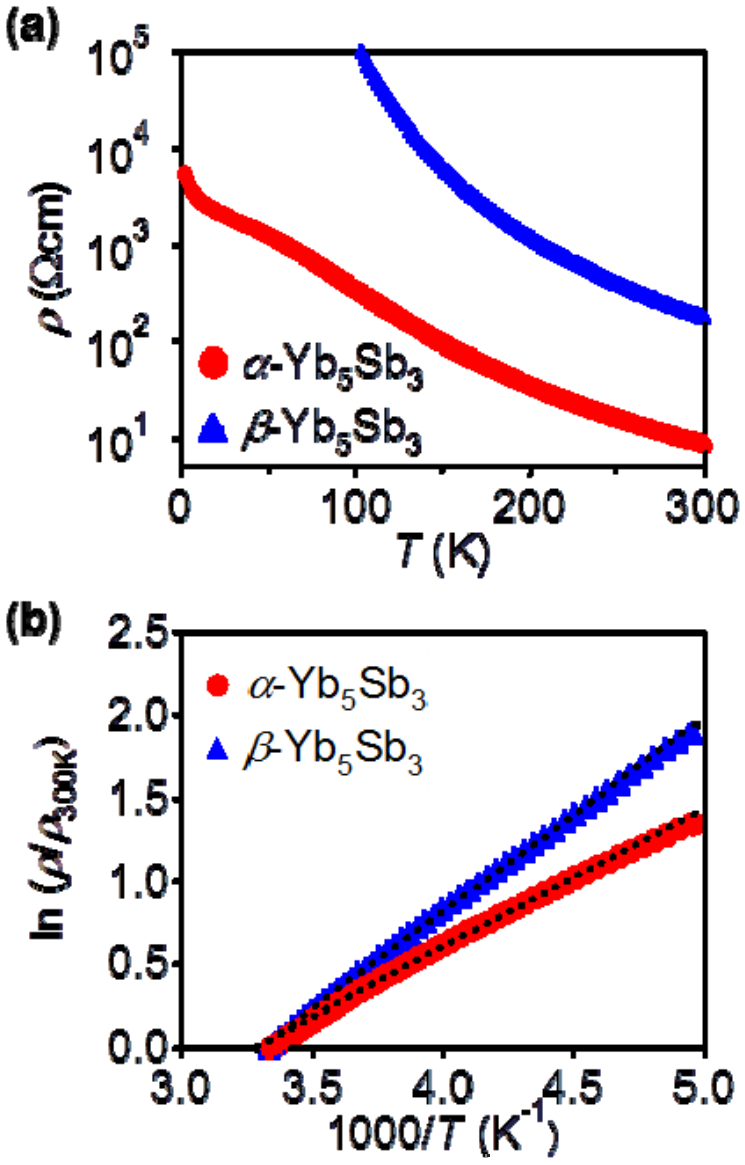
(a)
10^5
10^4
10^3
10^2
10^1
ρ (Ωcm)
α-Yb_5Sb_3
β-Yb_5Sb_3
0
100
200
300
T (K)
(b)
2.5
2.0
1.5
1.0
0.5
0.0
ln (ρ/ρ_{300K})
α-Yb_5Sb_3
β-Yb_5Sb_3
3.0
3.5
4.0
4.5
5.0
1000/T (K^{-1})

Figure 8

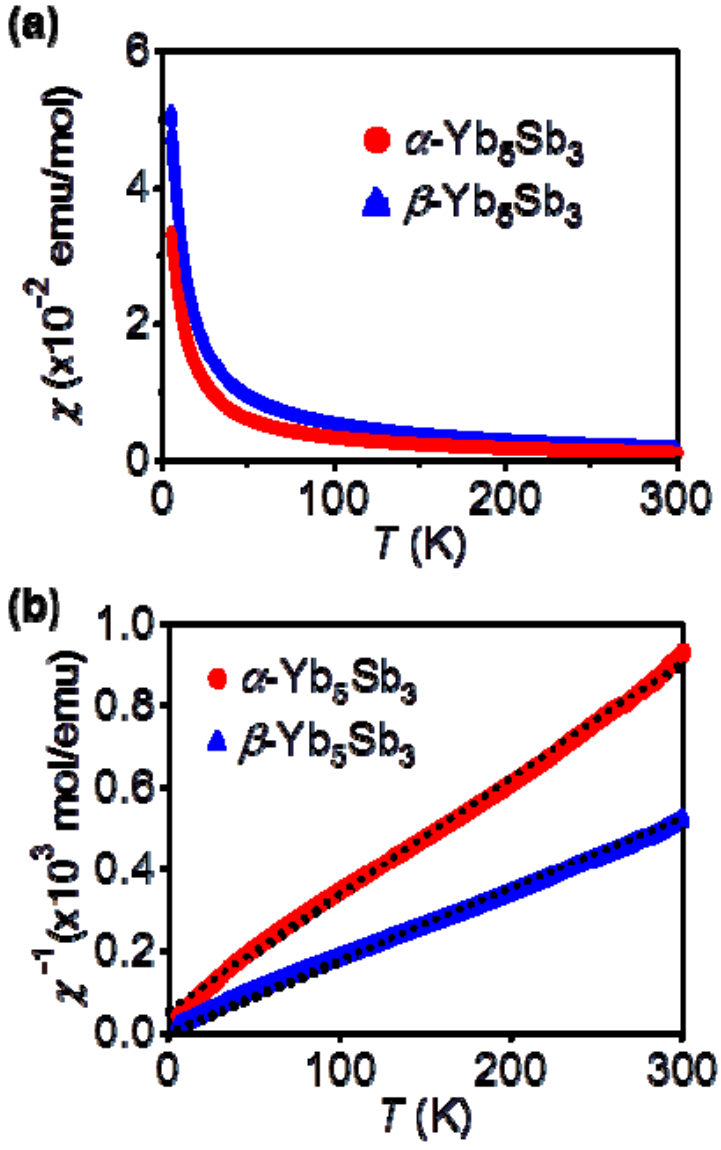
(a)
6
4
2
0
χ (x10^-2 emu/mol)
α-Yb5Sb3
β-Yb5Sb3
0
100
200
300
T (K)
(b)
1.0
0.8
0.6
0.4
0.2
0.0
χ^-1 (x10^3 mol/emu)
α-Yb5Sb3
β-Yb5Sb3
0
100
200
300
T (K)

Figure 9

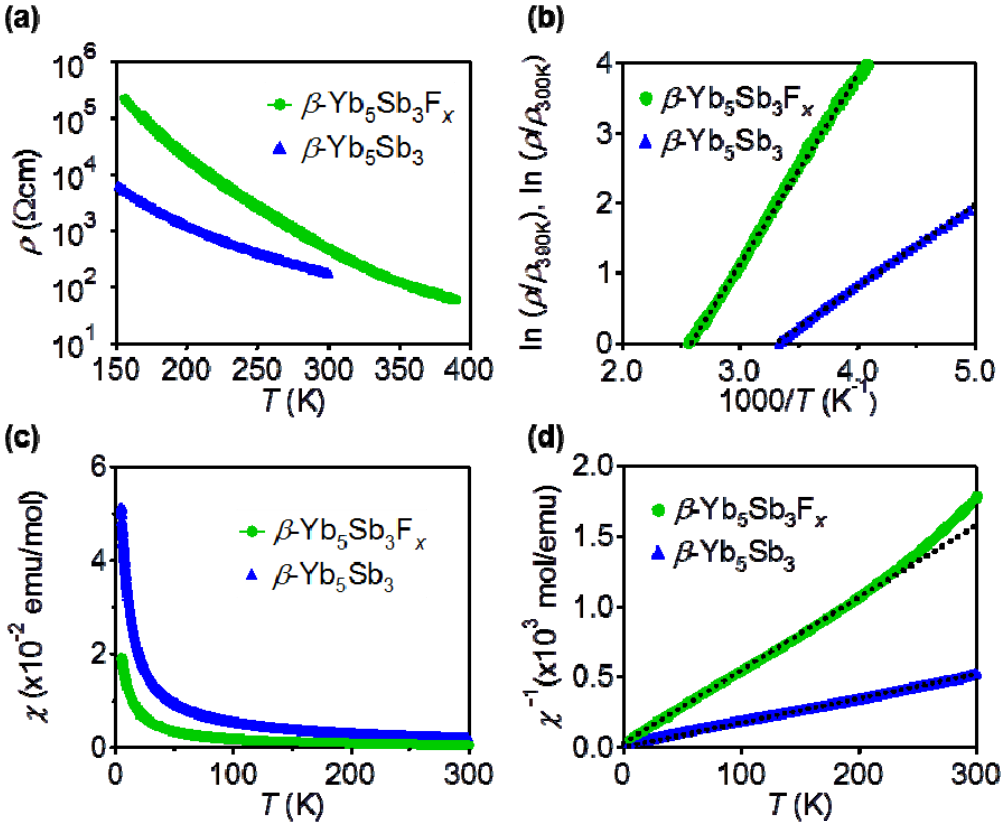
(a)
ρ (Ωcm)
T (K)
β-Yb5Sb3Fx
β-Yb5Sb3
(b)
ln (ρ/ρ300K), ln (ρ/ρ300K)
1000/T (K-1)
β-Yb5Sb3Fx
β-Yb5Sb3
(c)
χ (x10-2 emu/mol)
T (K)
β-Yb5Sb3Fx
β-Yb5Sb3
(d)
χ-1 (x103 mol/emu)
T (K)
β-Yb5Sb3Fx
β-Yb5Sb3

Figure 10

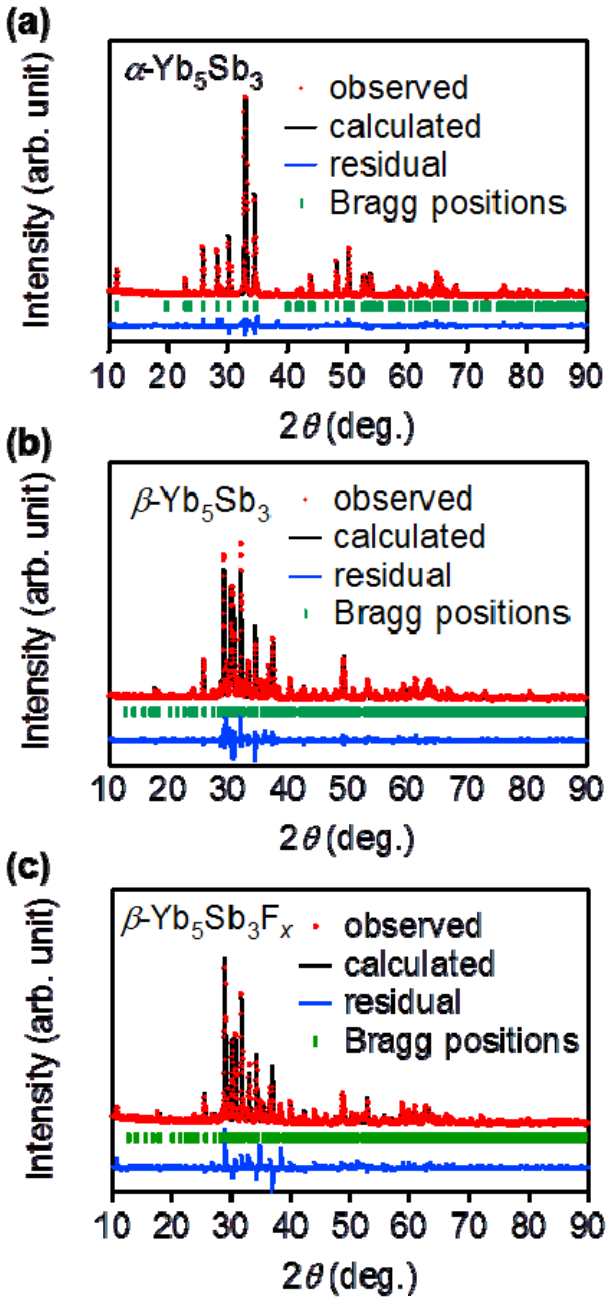
(a)
α-Yb5Sb3
observed
calculated
residual
Bragg positions
Intensity (arb. unit)
10 20 30 40 50 60 70 80 90
2θ (deg.)
(b)
β-Yb5Sb3
observed
calculated
residual
Bragg positions
Intensity (arb. unit)
10 20 30 40 50 60 70 80 90
2θ (deg.)
(c)
β-Yb5Sb3Fx
observed
calculated
residual
Bragg positions
Intensity (arb. unit)
10 20 30 40 50 60 70 80 90
2θ (deg.)

Figure 11

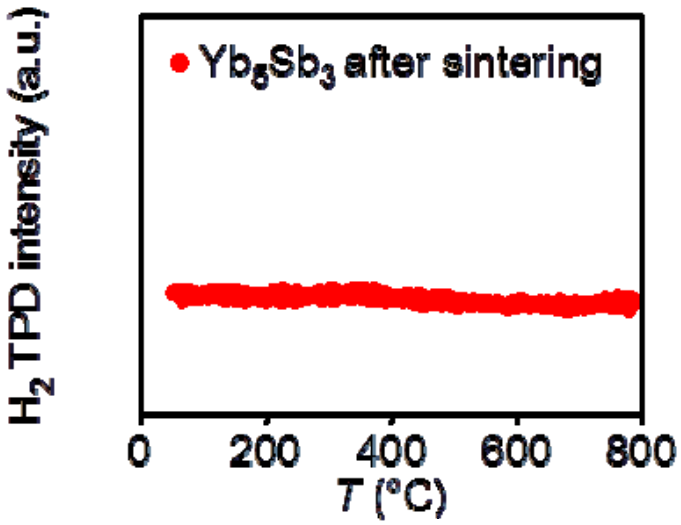
H_2 TPD intensity (a.u.)
Yb_5Sb_3 after sintering
0
200
400
600
800
T (°C)

Figure 12

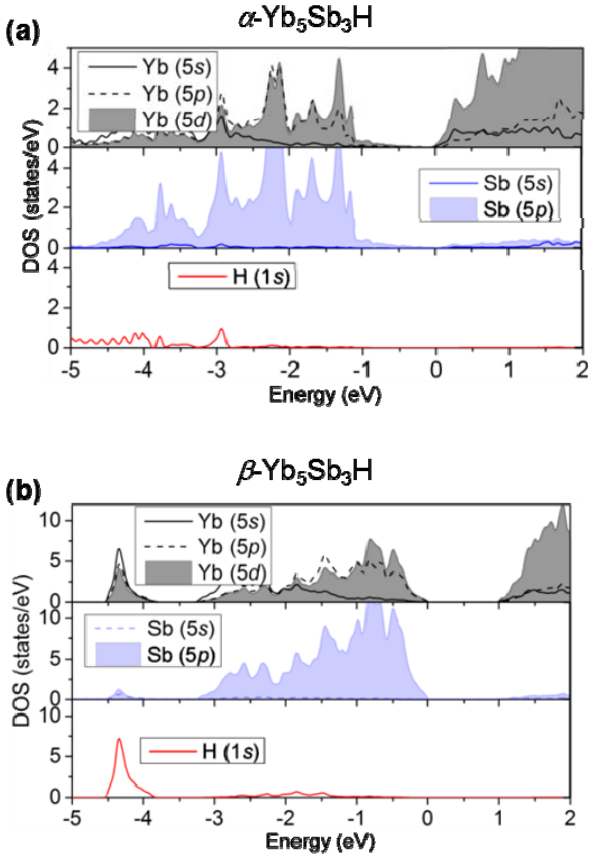
(a)
α-Yb5Sb3H
Yb (5s)
Yb (5p)
Yb (5d)
Sb (5s)
Sb (5p)
H (1s)
DOS (states/eV)
Energy (eV)
(b)
β-Yb5Sb3H
Yb (5s)
Yb (5p)
Yb (5d)
Sb (5s)
Sb (5p)
H (1s)
DOS (states/eV)
Energy (eV)

Figure 13

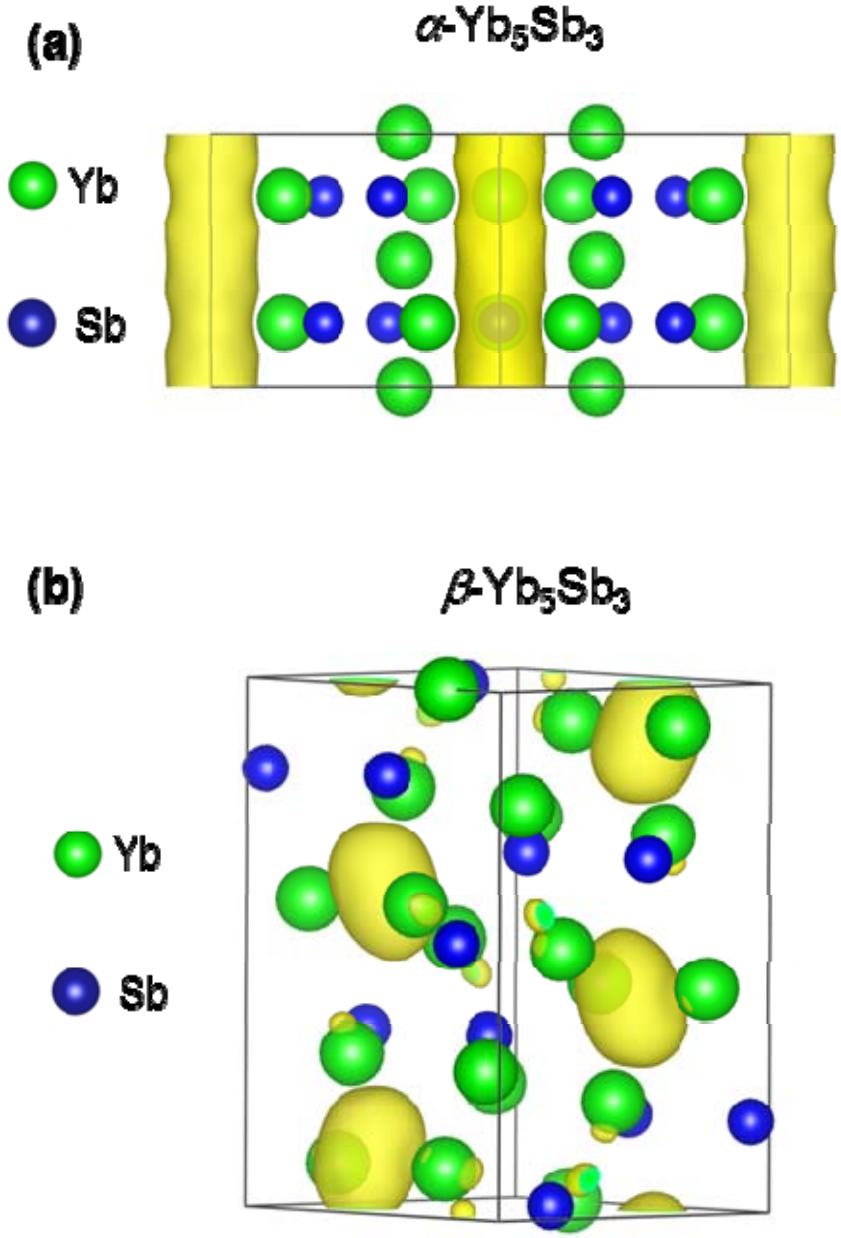

Figure 14

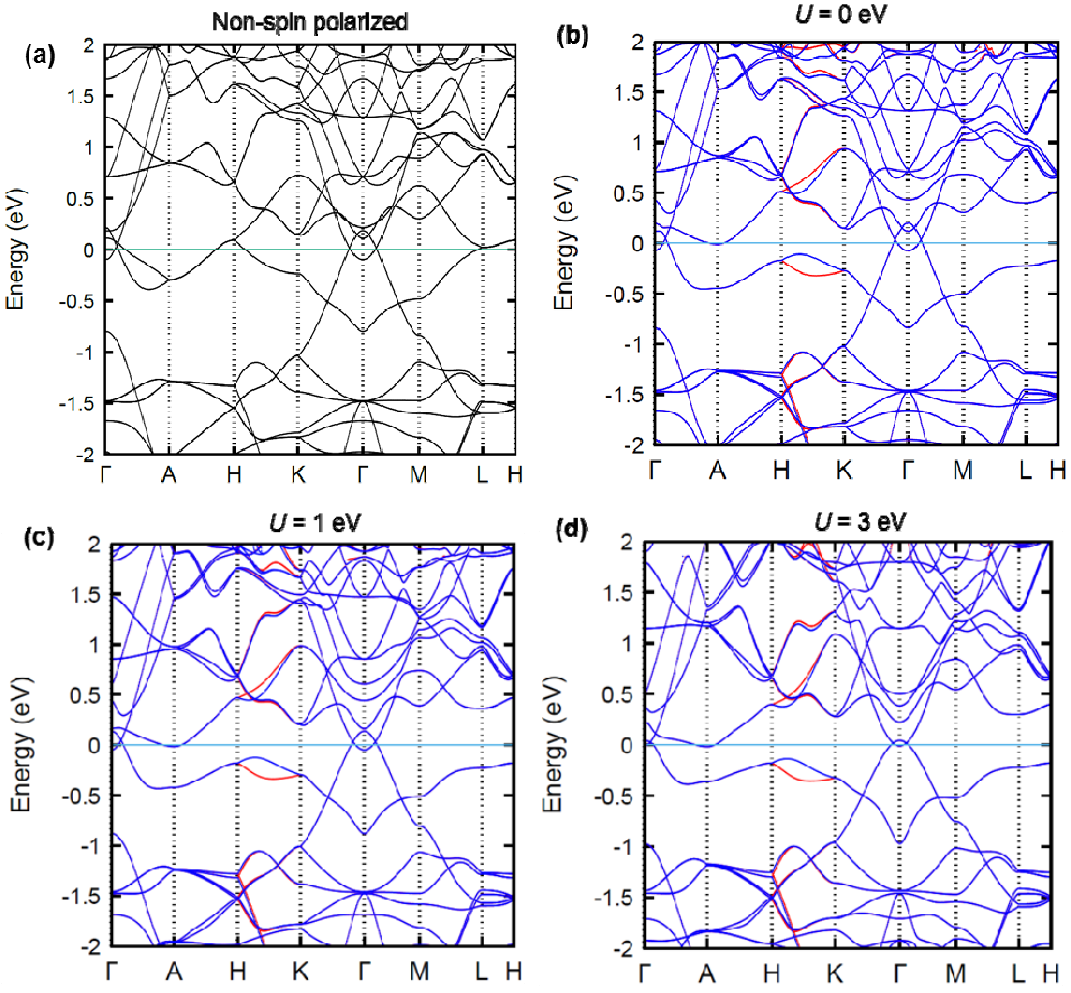
(a)
Non-spin polarized
(b)
U = 0 eV
(c)
U = 1 eV
(d)
U = 3 eV
Energy (eV)
2
1.5
1
0.5
0
-0.5
-1
-1.5
-2
Γ A H K Γ M L H

Figure 15

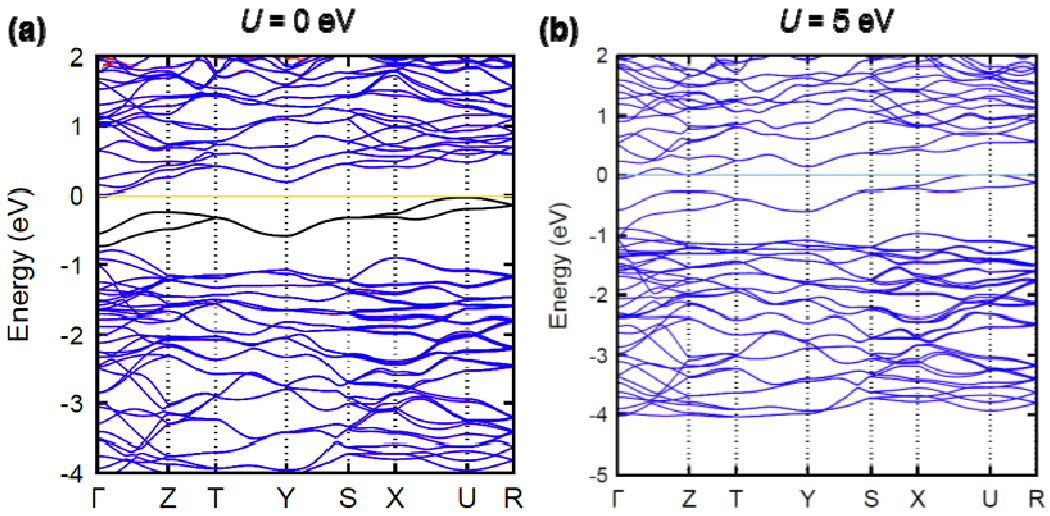

Figure 16

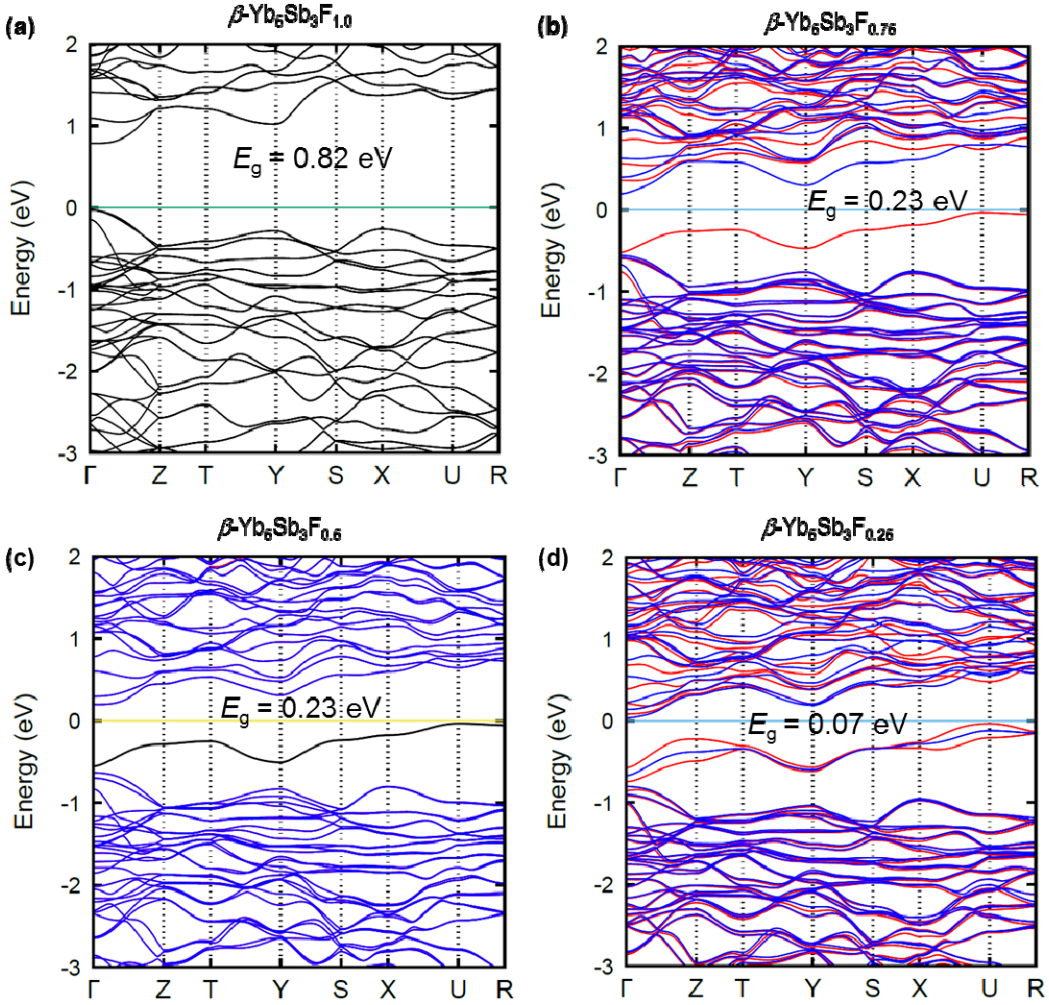
(a)
β-Yb6Sb3F1.0
Eg = 0.82 eV
(b)
β-Yb6Sb3F0.75
Eg = 0.23 eV
(c)
β-Yb6Sb3F0.5
Eg = 0.23 eV
(d)
β-Yb6Sb3F0.25
Eg = 0.07 eV
Energy (eV)
2
1
0
-1
-2
-3
Γ Z T Y S X U R

Figure 17

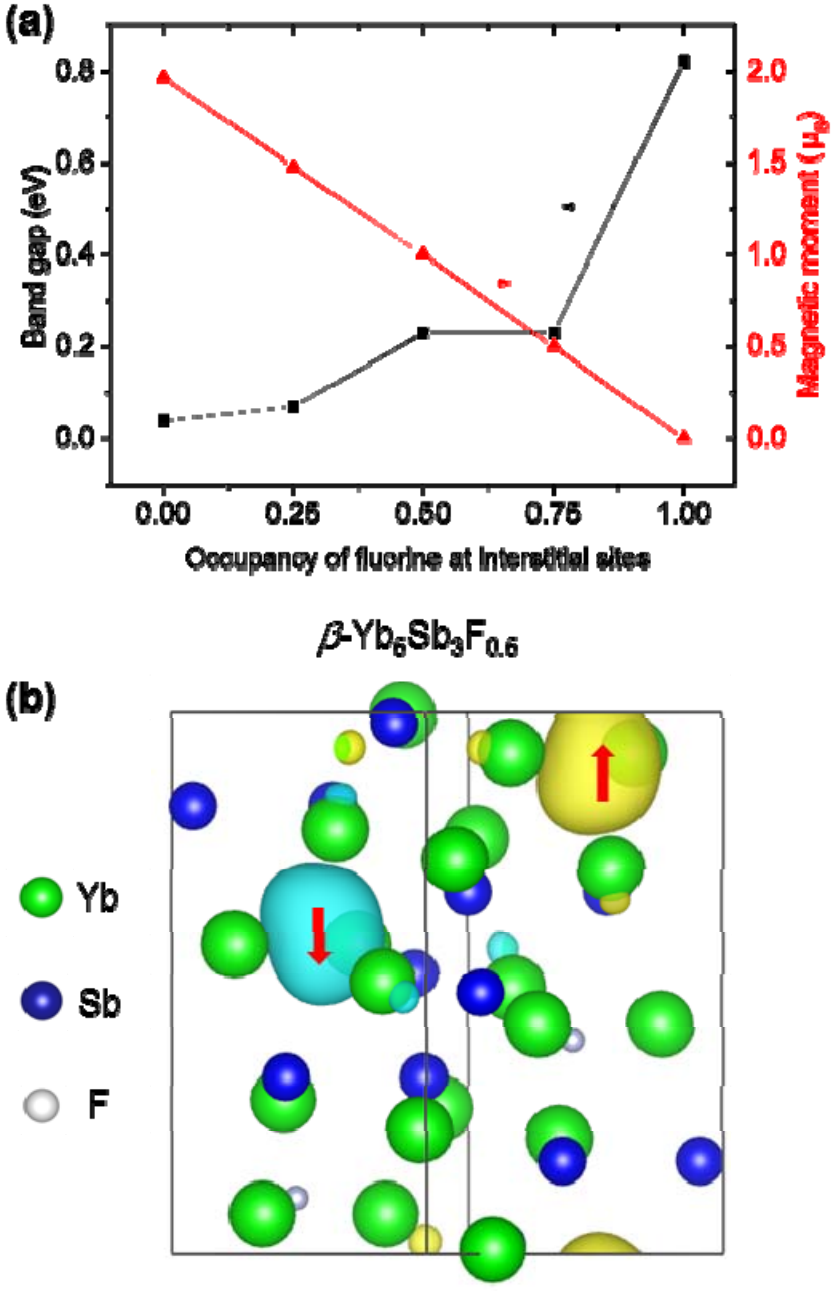
(a)
Band gap (eV)
Magnetic moment (μ_B)
Occupancy of fluorine at interstitial sites
0.0
0.2
0.4
0.6
0.8
0.0
0.5
1.0
1.5
2.0
0.00
0.25
0.50
0.75
1.00
β-$Yb_6Sb_3F_{0.6}$
(b)
Yb
Sb
F